RESEARCH ARTICLE

CrossMark

Stall cell formation over a post-stall airfoil: effects of active perturbations using plasma actuators

Ata Esfahani[1] · Nathan Webb[1] · Mo Samimy[1]

Abstract

Stall cells have been observed over stalled airfoils by many researchers and there have been extensive discussions in the literature on their formation mechanism. They have been known to be unsteady and sensitive to even the smallest upstream perturbations, and therefore, can be made spatially steady by fixing the upstream perturbation location. In the current experimental work, flow with a Reynolds number of $5 \cdot 10^5$ over a stalled VR-7 airfoil with an aspect ratio 3 was perturbed using a single nanosecond dielectric barrier discharge (NS-DBD) plasma actuator positioned near the leading edge and covering the span of the airfoil. Surface oil flow visualization and stereo particle image velocimetry were employed to investigate spanwise non-uniformities on the airfoil surface as well as in the flow. The results show a gradual appearance of stall cells by increasing the perturbation Strouhal number to approximately 3 times the natural shedding Strouhal number of $St_n = 0.6$ ($St_e \sim 3St_n$). The stall cells become well-defined and eventually saturated with no further changes with increasing perturbation Strouhal number beyond $10St_n$. The instability responsible for the stall cells is self-sustained as the stall cells persist after the perturbations are stopped. The results of the current work are discussed and interpreted using recent modal and non-modal linear global instability analyses, even though they are carried out in much lower Reynolds number laminar stalled flows over airfoils.

1 Introduction

Flow separation leading to stall imposes considerable performance penalties on lifting surfaces. Limitations of flight envelope and loss of control are among the chief reasons for the interest in the aerospace community for better understanding of this phenomenon. This problem is relevant to a wide range of applications from wind turbine to rotorcraft blades and from the wings of super-maneuverable fighter aircraft to agile micro air vehicles.

The stall characteristics of various airfoils are directly related to their geometry. Thick airfoils are known to undergo so-called gentle stall in the form of trailing edge separation which progressively moves towards the leading edge with increasing the angle of attack. Thin airfoils, on the other hand, experience what is commonly referred to as abrupt stall, where a sudden flow separation from the

leading edge leads to the abrupt loss of lift (McCullough and Gault 1951). The leading edge radius of curvature dictates the momentum required to maintain attached flow and this, in turn, shapes the stalling behavior of airfoils (Greenblatt and Wygnanski 2003). The emergence of three-dimensional flow features in post-stall regimes further complicates the stall phenomenon and leads to manifestation of effects such as lift and drag modulation and variation along the airfoil span (Spalart 2014; Ragni and Ferreira 2016).

The mushroom-shaped, three-dimensional flow features on the surface of a post-stall airfoil, referred to as stall cells, have been the subject of investigation for over 45 years with early reports of their appearance by Gregory et al. (1971) and Moss and Muradin (1971) on thick and thin airfoils, respectively. Further investigation of stall cells, all on thick airfoils, by Winkelmann and Barlow (1980), Weihs and Katz (1983), Boiko et al. (1996), Yon and Katz (1998a), Broeren and Bragg (2001), and Schewe (2001), using flow visualization techniques such as tufts and surface oil flow visualization, shed light on the conditions under which stall cells emerge. They also resulted in the derivation of empirical relations that could be used for predicting the number and wavelength of stall cells (Weihs and Katz 1983; Yon

✉ Mo Samimy
   samimy.1@osu.edu

[1] Gas Dynamics and Turbulence Laboratory, Aerospace Research Center, The Ohio State University, Columbus, OH 43235, USA

and Katz 1998a; Boiko et al. 1996; Disotell 2015). A better understanding of stall cells has been obtained recently through the use of advanced optical diagnostic techniques such stereo PIV and pressure sensitive paints. Studies by Manolesos and Voutsinas (2014), DeMauro et al. (2015), Dell'Orso et al. (2016a, b), Disotell and Gregory (2015), and Ragni and Ferreira (2016) have used two-component planar and stereo PIV, not only to determine the extent of the stall cells, but also to study their temporal evolution and obtain the distribution of vorticity and Reynolds stress concentrations within the flow field. Disotell et al. (2016) used fast-responding pressure sensitive paint to obtain the pressure distribution over a pitching wind turbine blade in the presence of stall cells. While advances in flow diagnostics have helped to further understanding of stall cells and their characteristics, the underlying mechanisms that lead to their emergence in post-stall flows are not yet well-understood. The most recent work (Dell'Orso and Amitay 2018) shows a strong dependence of spanwise three-dimensional features, including stall cells, on both Reynolds number and angle of attack for a NACA 0015 airfoil with an aspect ratio of 4.

Early work of Weihs and Katz (1983) postulated that stall cells are formed due to the excitation of the Crow instability (Crow 1970) whereby the interaction between the vortex lines shed from the shear layer over the separated region and the trailing edge of the airfoil leads to the formation of vortex rings which impinge on the airfoil surface and form stall cells. Yon and Katz (1998b), in their study, concluded that shear layer roll up is not the mechanism responsible for the formation of stall cells. Rodriguez and Theofilis (2011) performed modal linear global stability analysis aimed at exploring the formation mechanism of stall cells with a different approach. They perturbed a low-Reynolds number laminar flow over a stalled airfoil with two- and three-dimensional disturbances and used modal linear global stability analysis to calculate the global eigenmodes. They found that disturbances of any amplitude would induce three-dimensional features as the investigated flow was unstable due to the presence of the low-momentum reversed flow region. They produced surface topology similar to stall cells by linear superposition of the two-dimensional flow around the stalled airfoil and the dominant stationary three-dimensional global eigenmode excited by higher perturbation levels (Rodriguez and Theofilis 2011). Rodriguez and Theofilis (2010) used the same process in a separated two-dimensional boundary layer subjected to an adverse pressure gradient and produced structures similar to stall cells. The most recent modal and non-modal linear global stability analysis (He et al. 2017) of stalled laminar flows demonstrates that the problem is more complicated. They used stalled flows over three different types of airfoils (thin and thick with camber and thick without camber) to show that the Kelvin–Helmholtz (K–H) instability is more amplified than the stationary three-dimensional global mode of separation first discovered by Theofilis et al. (2000). He et al. (2017) produced flow structures similar to stall cells by superimposing the K–H mode on the stability analysis results of time-periodic base flow that resulted from the linear amplification of the K–H mode.

Interestingly, it appears that there are some common features of separated flows, regardless of Reynolds number or Mach number (Martin et al. 2016). First, they contain embedded streamwise structures or vortices, such as those generating stall cells in flows over stalled airfoils (Weihs and Katz 1983; Yon and Katz 1998b, Rodriguez and; Theofilis 2011; Manolesos and Voutsinas 2014; He et al. 2017), separated two-dimensional boundary layers (Rodriguez and Theofilis 2010) and Gortler-type streamwise vortices in supersonic (Martin et al. 2016) and hypersonic (Helm and Martin 2017) shock wave/turbulent boundary layer interactions. Second, the streamwise vortices are unsteady and sensitive to upstream disturbances, but they can be made spatially steady by fixing the location of upstream disturbances, as has been done in flows over stalled airfoils (Yon and Katz 1998b; Manolesos and Voutsinas 2014; DeMauro et al. 2015; Dell'Orso et al. 2016a, b) and in supersonic shock wave/turbulent boundary layer interactions (Schülein and Trofimov 2011). Third, there are two main unsteady features in the flow (Yon and Katz 1998b; Martin et al. 2016); one is associated with the shedding of vortices over the shear layer and another, which is of an order of magnitude smaller frequency, is likely associated with the unsteady separated-bubble motion. The exact mechanism for the latter is still being debated in the literature.

Plasma actuators have been used for active flow control in a wide variety of applications (Moreau 2007; Samimy et al. 2007, 2018; Benard and Moreau 2010). Dielectric barrier discharge (DBD) actuators driven by AC waveforms impart momentum to the flow, but the momentum scaling requirements prohibit them from being effective at the high Reynolds numbers typical of many applications (Patel et al. 2008; Roupassov et al. 2009). An alternative, first investigated by Roupassov et al. (2009), is to drive DBD actuators with high-voltage nanosecond DC pulses at various frequencies. These actuators have demonstrated control authority at relatively higher flow speeds (Adamovich et al. 2012; Marino et al. 2013; Peschke et al. 2013; Rethmel et al. 2011; Roupassov et al. 2009; Nishihara et al. 2011; Little et al. 2012) as their control mechanism is not momentum based. Many studies have demonstrated that nanosecond pulse driven DBD (NS-DBD) actuators mainly affect the flow by generating rapid, localized Joule heating that can excite the instabilities in the flow. This leads to the generation of coherent structures which promote mixing and otherwise alter the flow structure (Little et al. 2012; Dawson and Little 2013, 2014; Leonov et al. 2014; Akins et al. 2015). In particular, their bandwidth

makes them a flexible tool to alter the perturbation environment over a stalled airfoil. For detailed discussions on thermal-based plasma actuators, the readers are referred to Samimy et al. (2018) and Little (2018).

Our previous work on a thin, asymmetric airfoil investigating the effects of high-frequency excitation by NS-DBDs revealed some discrepancies between static pressure measurements and streamwise PIV measurements collected at different spanwise locations (Esfahani et al. 2016) hinting to spanwise three-dimensionality in the flow. The difference in location was to ease the optical access demands on the facility and was based on assumed nominally two-dimensional flow over the airfoil. A limited series of surface oil flow visualization experiments confirmed the existence of stall cells over the airfoil under various excitation frequencies.

This work seeks to explore the three-dimensional flow features on a thin, post-stall airfoil when the flow is actively perturbed over a wide range of Strouhal numbers. Development of 3-D features under excitation at various perturbation Strouhal numbers is studied using fluorescent surface oil flow visualization and stereo PIV. The data is then compared with streamwise planar PIV data from the previous study (Esfahani et al. 2016). Ensemble-averaged, cross-stream PIV data was acquired to elucidate the general features of the flow field. The implications of the presented findings are discussed.

2 Experimental facility and techniques

2.1 Airfoil and facility

Experiments were performed in the recirculating wind tunnel located at the Gas Dynamics and Turbulence Laboratory, within the Aerospace Research Center at The Ohio State University. The tunnel has an optically clear acrylic test section measuring 610×610 mm in cross-section and 1220 mm in length. A Boeing Vertol VR-7, a thin, asymmetric airfoil

typical in rotorcraft applications, was installed in the tunnel. The composite airfoil had a chord of $c = 203$ mm and was mounted in the center of the test section between the tunnel walls, giving it an aspect ratio $AR = 3$. The appearance of stall cells in stalled flows on airfoils mounted between tunnel walls (referred to as 2-D airfoils) was believed to be due to wall interactions (Winkelmann 1982). However, detailed experiments on finite span airfoils by Winkelmann (1982) and Winkelmann et al. (1982) indicated that stall cells emerge in stalled flows regardless of wall interactions, although the cell patterns formed on finite wings are different than the ones that appear on 2-D airfoils due to the interaction between the tip vortex and the stall cell(s). The airfoil in the current experiments is held in place between the two walls of the tunnel using two optically transparent acrylic disks that are imbedded in the tunnel walls and can rotate continuously, allowing for any angle of attack (α). The tunnel is capable of producing a continuous range of flow velocities from 3 to 95 m/s. Further details may be found in the works of Esfahani et al. (2016) and Little et al. (2012). The angle of attack (α) investigated here was 19° at a chord-based Reynolds number (Re) of $0.50 \cdot 10^6$. This α was chosen to avoid significant pressure fluctuations near the leading edge that were observed around the stall angle of 16° (shown later). The wind tunnel blockage due to the increased α is normally kept below 8% to avoid any increase in dynamic pressure, and therefore, increase in the moments and forces experienced by the model, particularly lift (Barlow et al. 1999). The blockage with 19° α, as in the current work, is 10.85%, which is larger than desirable. However, as will be further discussed later in the paper, α was kept constant in all the experiments conducted and only the perturbation frequency is changed. Therefore, any effect of blockage on the results presented in this paper is expected to be small. The freestream turbulence intensity is on the order of 0.25% at this Reynolds number.

Two coordinate systems are used throughout this paper. The first coordinate system, shown in Fig. 1, has its origin

Fig. 1 Schematic of the airfoil demonstrating the chosen coordinate origin and actuator location in the first coordinate system
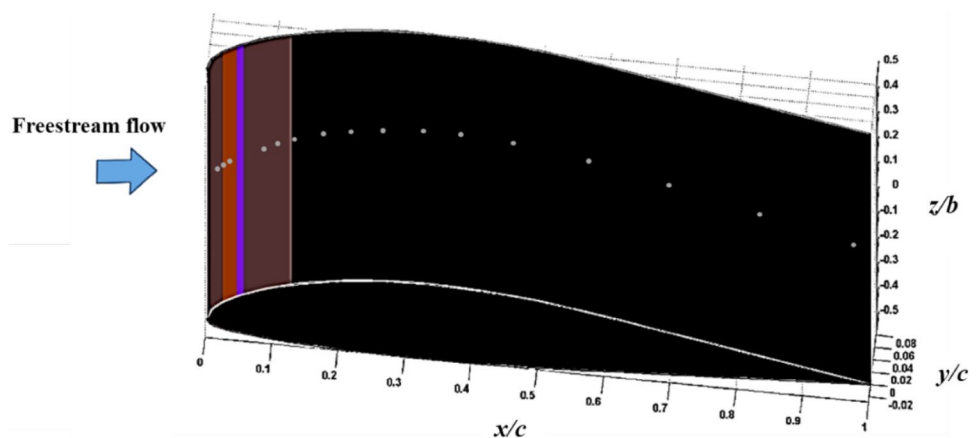
fixed at the airfoil leading edge. The system is a Cartesian grid aligned with the test section where streamwise (x) and normal axes (y) are normalized by the chord, denoted x/c and y/c and the spanwise axis (z) is normalized by the span ($b = 0.61$ m) denoted by z/b. The second system is in the test section reference frame, with its origin at the trailing edge of the airfoil and is used to present streamwise-planar and spanwise-stereo PIV data. Here, normal and spanwise axes are normalized by the chord and span, respectively, and are denoted by y/c and z/b.

2.2 NS-DBD actuator and pulser

A single actuator was placed close to the airfoil leading edge. The actuator was constructed of two 0.09 mm thick copper tape electrodes; the exposed high-voltage electrode is 6.35 mm (0.25 in) wide and the covered ground electrode is 12.70 mm (0.50 in) wide. The dielectric layer is composed of three layers of Kapton tape, each 0.09 mm thick with a dielectric strength of 10 kV. The total thickness of the entire actuator is 0.45 mm. The combination of covered electrode and dielectric layer was flush mounted with the surface of the airfoil. The actuator was placed on the suction side of the airfoil with the exposed electrode junction at $x/c = 0.04$. This location was just upstream of the edge of the separation line, for the clean baseline airfoil, as determined by surface oil flow visualization.

The nanosecond pulse waveform used to drive the actuator is generated by a custom, in-house built pulse generator that utilizes a magnetic compression circuit. A DC, 450 VDC power supply was used to power the pulse generator. The specifics of the pulse generator are discussed in previous work by Little et al. (2010) and Takashima et al. (2011).

Representative discharge characteristics were acquired for an approximately 570-millimeter-long actuator driven at 100 Hz. The voltage (V) and current (I) traces of a typical discharge, in addition to the power and instantaneous energy traces, are plotted in Fig. 2. The peak voltage was 10 kV and the peak current was 36 A. Due to the very narrow pulse width, the energy consumption was 12.6 mJ per pulse, which translates to 0.02 mJ/mm energy density. The natural shedding Strouhal number (St_n) was 0.6 (Esfahani et al. 2016). The perturbation Strouhal number, $St_e = f_e c / U_\infty$, was varied from 0.3 (= 0.5St_n) to 14.52 (= 24.2St_n), where f_e is the excitation frequency, c is the airfoil chord, and U_∞ is the freestream velocity.

2.3 Particle image velocimetry

PIV is the primary diagnostic technique employed in this work and data were acquired for both the flow over the suction side of the airfoil and behind the trailing edge. Maps of the normalized total velocity ($U^* = |U|/U_\infty$) and streamwise component of velocity ($u^* = u/U_\infty$) are used to investigate the flow.

The seed particles were injected upstream of the test section. Olive oil was atomized using a TSI 6-jet atomizer (model 9306A). The seed particles are illuminated using a Spectra Physics PIV-400 double-pulsed Nd:YAG laser. The laser beam is formed into a sheet by a 1 m focal length spherical lens and a 25 mm focal length cylindrical lens. Various turning optics were used to direct the laser sheet into the wind tunnel. The laser sheet has a thickness of approximately 2 mm.

To acquire streamwise data over the airfoil and in the wake region, a two-camera setup (shown in Fig. 3a) was
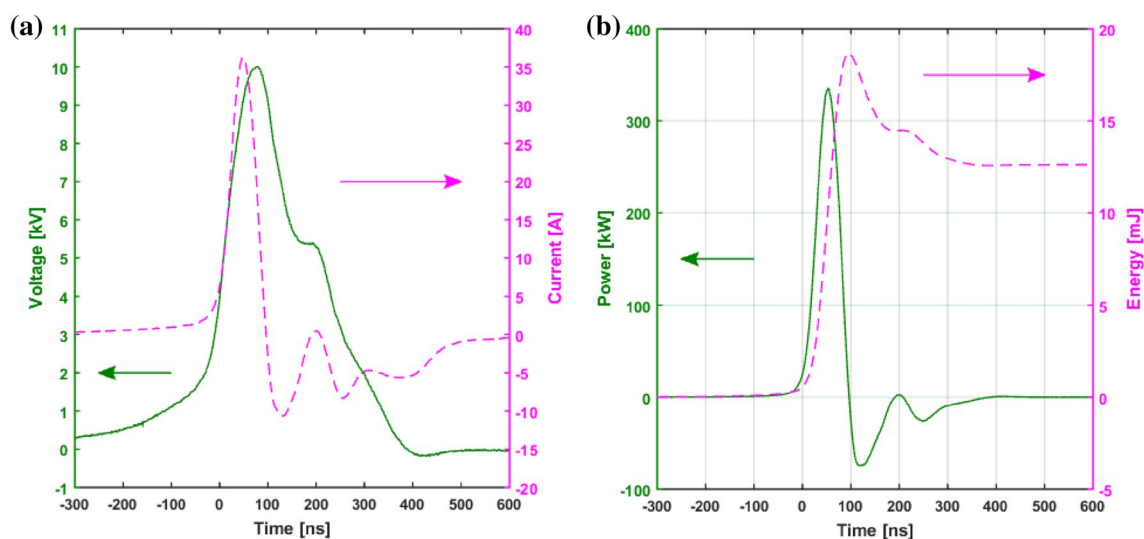

Fig. 2 Discharge characteristics of actuation: traces of instantaneous (**a**) current and voltage, **b** power and energy
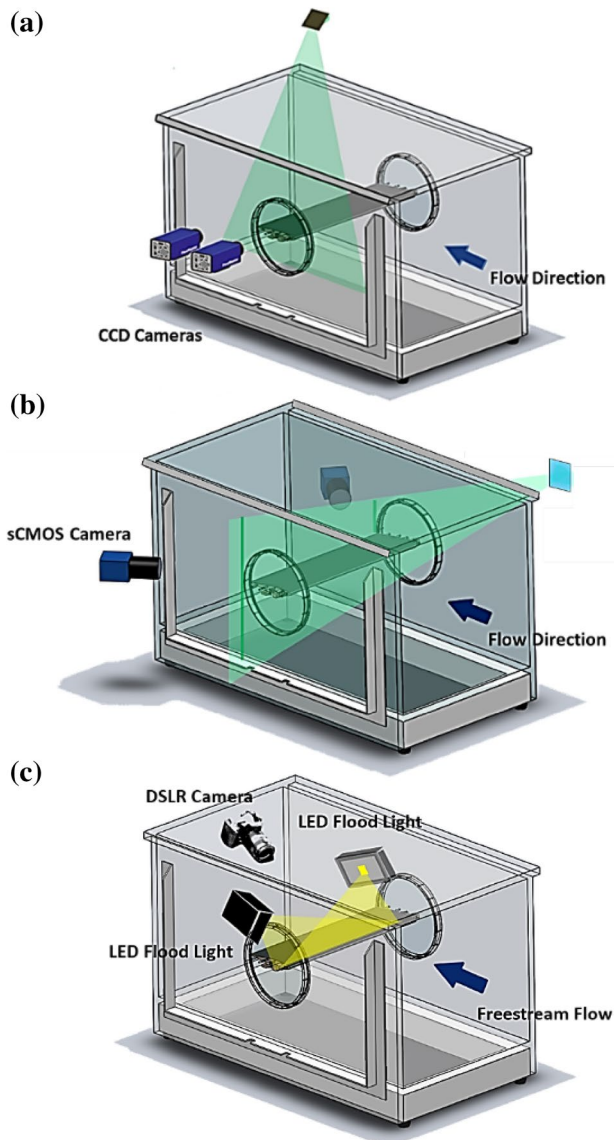
(a)

(b)

(c)

Fig. 3 Schematic of the optical diagnostic apparatuses used to characterize the flow (**a**) dual-camera streamwise-planar PIV setup with laser sheet at $z/b = -0.2$ and **b** spanwise-stereo PIV setup with laser sheet at $x/c = 1.05$. **c** Surface oil flow visualization setup

used to expand the streamwise field of view. The setup was comprised of two LaVision 12-bit 2048×2048 px Imager Pro camera bodies, each with a Nikon Nikkor 35 mm $f/1.2$ lens. The cameras were positioned 253 mm center to center on a horizontal optical rail. The lenses of the cameras were located approximately 980 mm from the laser sheet. In this arrangement, the laser sheet was located at $z/b = -0.2$ (the laser sheet could not be placed at $z/b = 0$ due to optical access limitations). The cameras acquired data simultaneously at an average acquisition rate of 3.3 Hz. For excited cases, five sets of 100 image pairs were taken for a given case, whereas for

the baseline data, a single set of 1000 images were taken. The difference is due to the limited actuator run time.

A stereo cross-stream PIV setup, seen in Fig. 3b, was employed to investigate flow non-uniformities in the spanwise direction. The stereo PIV setup was comprised of two 5.5-megapixel, 16-bit LaVision Imager sCMOS cameras. Each camera was fitted with a 24 mm, wide-angle Nikon Nikkor f/2.8 lens to maximize the field of view. Approximately 89% of the airfoil span was imaged with this setup. The angle between the camera sensor normal vector and the tunnel centerline was approximately 37°. One set of 600 image pairs was acquired at a rate of 10.5 Hz for each data point.

2.4 Fluorescent surface oil flow visualization

Fluorescent surface oil-flow visualization (FSOFV) was employed to study the flow topology over the airfoil under various conditions. A mixture of 1000 and 350 cSt silicone oil (3 parts 1000 cSt oil and 7 parts 350 cSt oil) with a viscosity of approximately 480 cSt was used to hold the fluorescent pigments. The viscosity of the oil was chosen to allow the observation of unsteadiness in separation line location and simultaneously prevent excessive amounts of the mixture from flying off the model.

The UV pigments had an average diameter of 5–20 µm and could be excited by visible light. Two 1000 W LED flood lights were used to illuminate the mixture (as shown in Fig. 3) in 10-s intervals. The procedure for acquiring the images was as follows: first the angle of attack was set and the tunnel was brought up to speed. As soon as the desired conditions were established in the tunnel, the actuators were turned on. The final oil flow pattern was usually established after approximately 6 min of run time. Laboratory lights were then turned off and a DSLR camera was used to acquire the images in low- (ambient) light conditions. The acquired images were de-skewed and plotted using MATLAB.

2.4.1 Static pressure

Static pressure measurements on the airfoil surface were acquired using three Scanivalve digital pressure sensor arrays (DSA-3217). A total of 35 taps are located on the surface of the airfoil three of which between $x/c = 0.05$ and 0.1 are covered by the DBD actuator. As such, data from these taps is ignored. The pressure coefficient, $C_p = (p - p_\infty)/q_\infty$, was averaged over 300 samples acquired at 1 Hz near the centerline; p, p_∞, and q_∞ are static pressure at the measurement location, freestream static pressure, and freestream dynamic pressure. The sectional lift coefficient was calculated using the following line integral

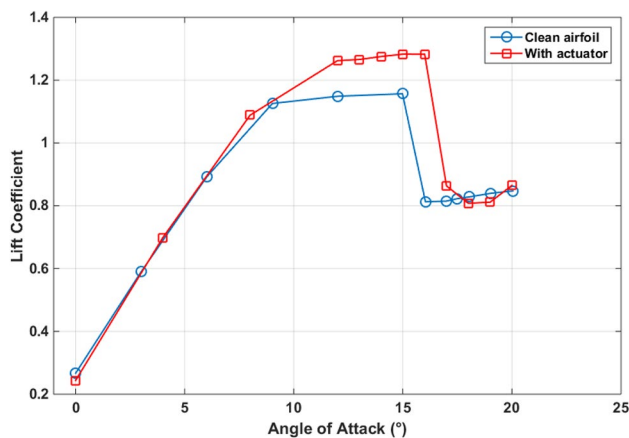$$C_l = -\int_{-1}^{1} C_p \sin\theta \, ds, \tag{1}$$

Fig. 4 Variation of lift coefficient C_l vs. α at $Re = 500,000$

where θ is the surface-normal angle and ds is the arc length.

3 Results and discussion

3.1 Baseline mean flow features

The variation in lift coefficient of the baseline model, with and without the actuator electrode, with respect to α at $Re = 0.5 \times 10^6$ is shown in Fig. 4. It is evident that the stall angle for the clean VR-7 airfoil at this Reynolds number is 15°. The airfoil demonstrates the typical stalling behavior expected from thin airfoils (McCullough and Gault 1951; Greenblatt and Wygnanski 2003), specifically, a rapid drop in lift coefficient C_l due to abrupt leading edge flow separation is observed at this Reynolds number. Due to the relatively high α, the model blockage effects, both solid blockage and wake blockage, were deemed to be significant and expected to result in an increase in dynamic pressure, and therefore, an increase in the moments and forces experienced by the model, particularly lift (Barlow et al. 1999). As was mentioned earlier, the blockage with $\alpha = 19°$ in the current work is 10.85%, which is significantly larger than desirable. However, α was kept constant in all the PIV and surface flow visualization experiments conducted and only the perturbation Strouhal number was changed. Therefore, the observed changes in the flow are certainly due to the effects of perturbations and the changes in the perturbation Strouhal number.

While no changes in the lift coefficient magnitude are observed at lower angles of attacks ($0° < \alpha < 9°$), an average increase of more than 10% from $\alpha = 11°$ up to the stall angle is observed when the actuator is added close to the leading edge of the airfoil. Even though the exposed electrode of the actuator is 0.09 mm thick, its junction is at $x/c = 0.04$, where the boundary layer is very thin. Therefore, it could have a significant effect on the flow characteristics and the

lift coefficient. It must be noted also that 3 pressure taps located at $x/c < 0.1$ are covered when the actuator electrode is present and 2 taps close to the leading edge are covered without the presence of the actuator electrode. Since most of the lift in this airfoil is generated close to leading edge, the loss of pressure taps could also affect the accuracy of the lift coefficient magnitude in both cases. Furthermore, surface oil flow visualization experiments for the baseline and clean airfoils, to be discussed later, indicated that some three-dimensionality in the separation line location exists at higher angle of attacks. Consequentially, the separation line may or may not fall downstream of the covered pressure taps and as a result, the suction peak may or may not be registered in the pressure data. In addition, the separation line may be in different positions with respect to the line of pressure taps (shown later) for the two cases. Moreover, small variations in stall angle (about 1°) were observed when data was retaken multiple times. The combination of these effects could explain the discrepancies in the lift coefficient data with and without an actuator. However, all the results with and without the excitation presented in the remaining of the paper are obtained using the airfoil with the actuator in place. Therefore, the baseline and excited PIV and surface flow visualization results are free of these issues and can be compared.

It was deemed necessary to investigate the effect of installing the actuator on the surface topology. A comparison between the clean baseline airfoil and the one with the actuator installed is made in Fig. 5. The surface topology of the clean airfoil (Fig. 5a) shows the existence of two strong spiral nodes at $z/b = -0.37$ and 0.37. Although flow separates at approximately $x/c = 0.05$, a pattern that emerges further downstream across the span due to increased surface shear stress might be mistaken for a separation line. The
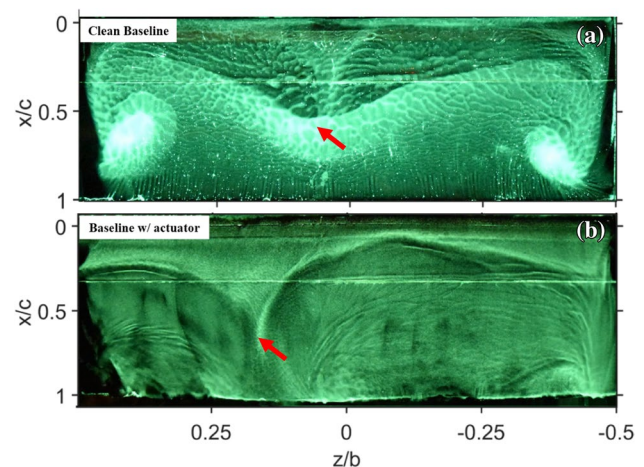

Fig. 5 Baseline fluorescent surface oil flow visualization images at $\alpha = 19°$ and $Re = 500,000$ for **a** clean airfoil and **b** airfoil with actuator installed, but inactive

overall surface topology pattern resembles the one referred to as "3-D separation with mid-span variation, type 2" by Dell'Orso and Amitay (2018) in their detailed parametric surface topology versus α research over a NACA 0015 airfoil at different Reynolds numbers. They referred to this surface pattern as a transitory pattern that is a precursor to the emergence of two, well-defined stall cells with four spiral nodes. Their investigation further indicates that the surface pattern of Fig. 5a is observed at high, post-stall angles of attack at a Reynolds numbers slightly less than the critical Reynolds number, at which, at a fixed α, stall cells appear. So, further increases in Reynolds number would likely result in the emergence of a two-cell pattern.

An examination of the FSOFV data for the baseline flow with the actuator installed presented in Fig. 5 indicates that a quasi-3-D separation front exists over the airfoil. Based on the above discussion, it appears that the presence of an actuator (Fig. 5b) results in an overall decrease in surface shear stress. Consequently, the onset of separation at mid-span (marked in Fig. 5 with an arrow) moves slightly upstream and to the left and the spiral nodes are weakened significantly. Similar 3-D separation front was observed by Disotell (2015), DeMauro et al. (2015) and Dell'Orso et al. (2016a, b) and suggested to be precursors to the development of well-defined mushroom-shaped structures. As was discussed earlier, these separated flows with a thin approaching boundary layer are highly susceptible to any minor surface imperfection (Yon and Katz 1998b; Manolesos and Voutsinas 2014, Schulein and; Trofimov 2011). Potential surface imperfections in the current research could have been introduced due to physical presence of the exposed electrode installed near the leading edge. A hint of potentially very weak spiral nodes at $z/b = 0$ and -0.5 may be present in the FSOFV image of the baseline model in Fig. 5b.

3.2 Effect of perturbations on the mean flow features

As was discussed earlier, the active perturbations in this work are generated using NS-DBD plasma actuators. Though the actuator frequency was varied, the energy per pulse was kept constant at 12.6 mJ. The natural shedding Strouhal number (St_n) was 0.6 (Esfahani et al. 2016). The perturbation Strouhal number, $St_e = f_e c / U_\infty$, changed from 0.3 ($0.5 St_n$) to 14.52 ($24.2 St_n$), as shown in Table 1, where f_e is the excitation frequency, c is the airfoil chord length, and U_∞ is the freestream velocity. The modal linear global stability analysis of Rodriguez and Theofilis (2011) in a laminar stalled flow over an airfoil showed the globally unstable nature of such flow and the dependence of the formation of the stall cells on the amplitude of the perturbations. However, the most recent modal and non-modal linear global stability analysis over three different airfoils (thin and thick

Table 1 Strouhal number for all 10 perturbed cases used in this paper

Case number	Baseline	1	2	3	4	5	6	7	8	9	10
Perturbation Strouhal number (St_e)	–	0.3	0.6	0.78	2.04	4.27	6.0	9.68	10.73	14.52	10.97 carrier signal modulated with 0.6 signal

without camber, and thick with camber), again in laminar stalled flows, showed that the Kelvin–Helmholtz instability (K–H) mode is amplified more strongly than the three-dimensional global mode and the stall cell-like structures are formed by superposition of the K–H and a secondary stability analysis results. As will be discussed in a more detail in Sect. 3.3, the K–H instability is known to amplify perturbations over a large range of Strouhal numbers and the perturbation amplitude does not play a significant role beyond a threshold level (Samimy et al. 2018).

The effects of perturbation St_e for all 10 cases listed in Table 1 are presented and discussed in this paper. Figure 6 shows the airfoil surface topology for the baseline flow with the installed actuator and two excited cases. Figures 7 and 8 show spanwise maps of normalized velocity distribution downstream of the trailing edge at $x/c = 1.05$ for the baseline flow with the installed actuator and two excited cases. In Fig. 8, the inset images show the total normalized velocity U^* at a streamwise plane at $z/b = 0.45$. Dashed black lines indicate ensembled-averaged zero streamwise velocity and can be used to assess separation height at each spanwise location.

The asymmetric surface pattern of the baseline develops into two asymmetric mushroom-shaped stall cells for low St_e in Case 2 (Fig. 7b). The spanwise PIV data does not indicate the presence of stall cells (Fig. 7b), but the SOFV clearly indicate that stall cells have formed under
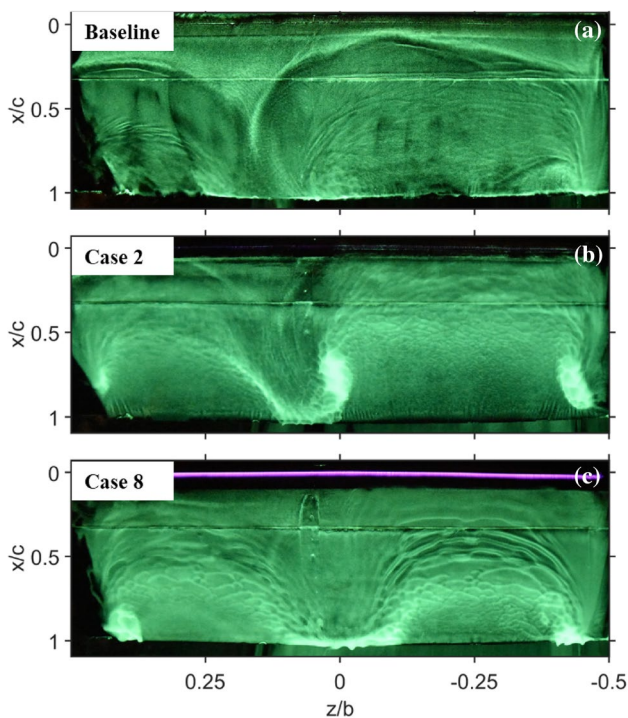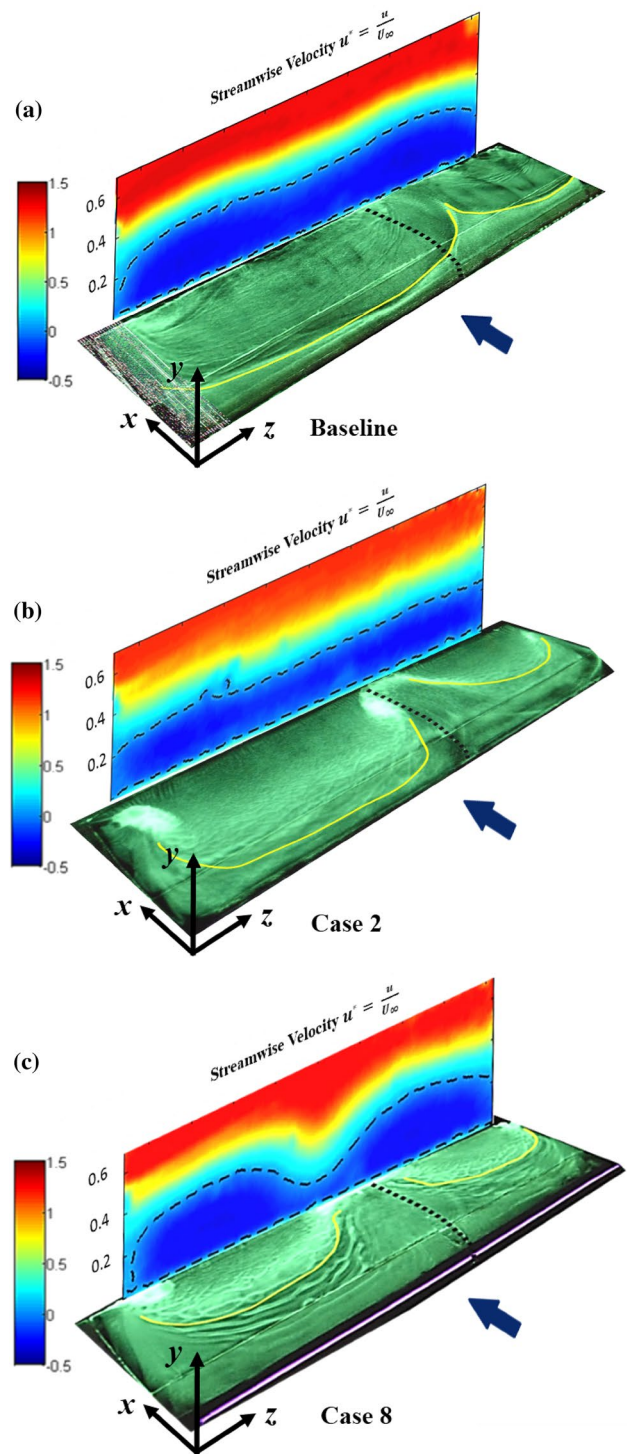

Fig. 7 Comparison between maps of normalized ensemble-averaged streamwise component of velocity u^* on a cross-stream plane at $x/c = 1.05$ and FSOFV images for $\alpha = 19°$ and $Re = 500,000$, for **a** Baseline, **b** Case 2, and **c** Case 8. Dashed black lines indicate zero streamwise velocity

Fig. 6 Fluorescent surface oil flow visualization at $\alpha = 19°$ and $Re = 500,000$. **a** Baseline, **b** Case 2, and **c** Case 8

(a)
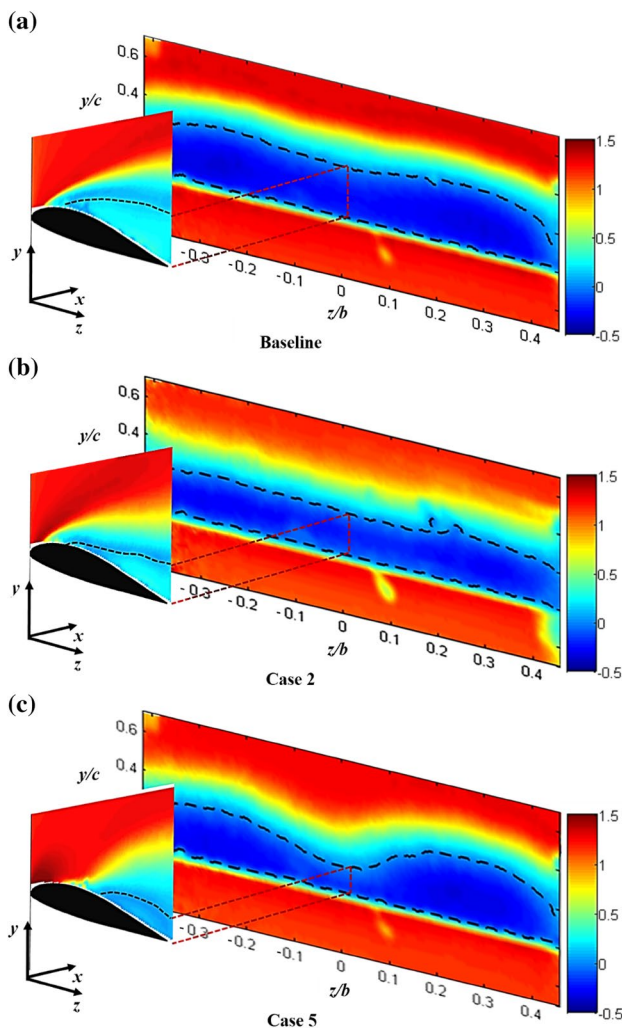

Baseline

(b)

Case 2

(c)

Case 5

Fig. 8 Comparison between maps of normalized ensemble-averaged streamwise component of velocity u^* on a cross-stream plane at $x/c = 1.05$ and total normalized velocity U^* on a streamwise plane at $z/b = 0.45$ (inset images) for $\alpha = 19°$ and $Re = 500,000$, for **a** baseline, **b** Case 2, and **c** Case 5. Dashed black lines indicate zero streamwise velocity

this condition. Previous work has shown that excitation at this Strouhal number, which is near the natural shedding Strouhal number ($St_n = fc/U_\infty \sim 0.6$) for the baseline case, generates coherent flow structures in the shear layer over the separated region that entrain high-momentum freestream flow into the separated zone and thus reduce the average separation height by bringing the zero-velocity line closer to the airfoil surface. They also reduce the magnitude of the reversed flow in the separation zone (Esfahani et al. 2016). A similar process normally occurs in the baseline case as well, with a natural shedding Strouhal number of 0.6 in the current work. The reason for this seeming discrepancy is related to the unsteady, cyclic formation and shedding of large-scale structures over the airfoil at $St_e = 0.6$ and the

unsteady, cyclic flow attachment and separation resulting in the mean velocity field shown in Fig. 7b. However, the flow on the surface is primarily affected by organized large-scale motions in the flow and thus SOFV image shown in Fig. 7b reflects their signature, while the flow field shown in Fig. 7b reflects all the flow fluctuations (organized and unorganized, small and large).

As the perturbation St_e is increased, the stall cells become more well-defined, as shown in Fig. 7c (Case 8). This can be further inferred by comparing zero-velocity lines in stream-wise maps of excited flow for Cases 8 and 5, in Figs. 7c and 8c, respectively. Two spiral nodes at $z/b = -0.4$ and -0.1, seen in the FSOFV image of Fig. 7c, are the footprints of streamwise vortices, embedded in the shear layer, that are responsible for this effect as suggested by analysis of stereo PIV data in Ragni and Ferreira's work (2016). Significantly increasing the perturbation St_e leads to the spanwise modulation of streamwise velocity and emergence of two well-defined asymmetric stall cells, as can be seen in Fig. 7c (Case 8) and Fig. 8c (Case 5). As will be shown later, this change in flow topology seems to begin to occur with Case 4 ($St_e = 2.04$). The separation height, measured at $z/b = 0$, is also significantly reduced for high St_e cases compared to the baseline case (Fig. 7c).

To better ascertain the dependence of the three-dimensionality of the flow field and the existence of stall cells on the perturbation St_e, spanwise maps of ensemble-averaged normalized streamwise-component of velocity distribution downstream of the trailing edge at $x/c = 1.05$ are shown in Fig. 9 for the baseline and for the 9 unmodulated cases listed in Table 1. Dashed black lines indicate zero streamwise velocity and can be used to assess time-averaged separation height at various spanwise locations. Exciting the flow at the lowest perturbation St_e (Case 1) results in a nearly two-dimensional distribution of velocity as is seen in Fig. 9b. The vertical extent of the reversed flow is somewhat reduced as is the normalized streamwise velocity from $y/c = 0.4$ to 0.6. The two-dimensional velocity distribution remains similar, but the reduced extent of the reversed flow and stream-wise velocity from $y/c = 0.4$ to 0.6 is accentuated when the perturbation St_e is further increased (Fig. 9c/Case 2, d/Case 3). These effects have been attributed to coherent large-scale structures generated by the low Strouhal number perturbation, which entrain high-momentum freestream flow into the separated region (Esfahani et al. 2016). The large vertical-velocity component (not shown) supports this assertion.

Further increase of the perturbation St_e to Case 4 (Fig. 9e) and beyond results in the emergence of two asymmetric stall cells with the right-hand cell having a slightly larger separation height than the left-hand one. A similar asymmetric pattern has also been observed by several previous researchers (Winkelmann and Barlow 1980; Yon and Katz 1998a; DeMauro et al. 2015; Disotell and Gregory
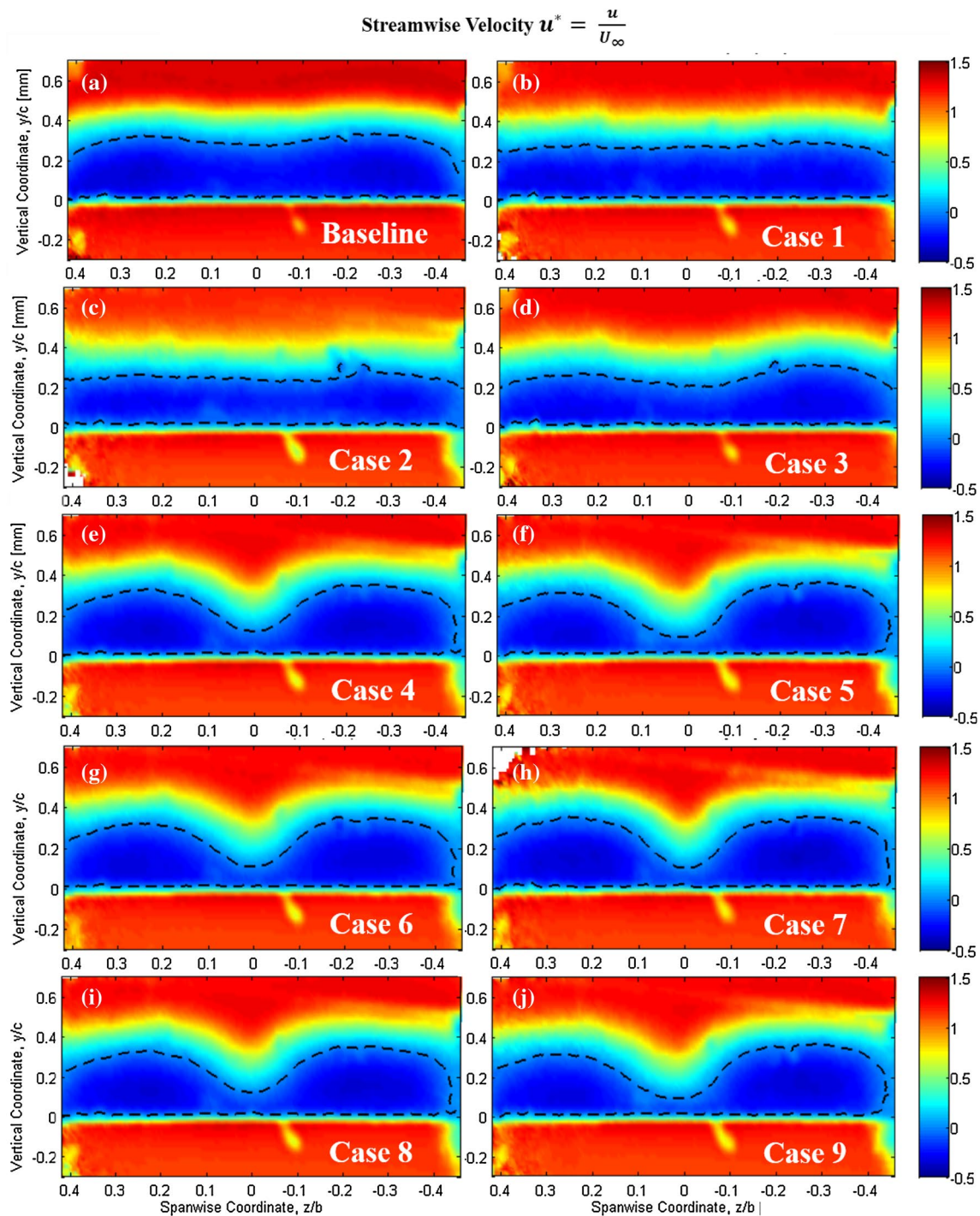
$$\text{Streamwise Velocity } \boldsymbol{u}^* = \frac{\boldsymbol{u}}{\boldsymbol{U}_\infty}$$

Fig. 9 Color maps of normalized, ensemble-averaged streamwise component of velocity u^* on a cross-stream plane at $x/c = 1.05$ for $\alpha = 19°$ and $Re = 500,000$ at the baseline and 9 perturbed cases listed in Table 1. Dashed black lines indicate zero streamwise velocity

2015; Dell'Orso et al. 2016a, b). As was discussed earlier, the streamwise flow features are unsteady and sensitive to upstream disturbances, and they can be made spatially steady by fixing the location of upstream disturbances, as has been done in flow over stalled airfoils (Yon and Katz 1998b; Manolesos and Voutsinas 2014, De Mauro et al.

2015; Dell'Orso et al. 2016a, b); and in supersonic shock wave/turbulent boundary layer interactions (Schulein and Trofimov 2011). Any potential surface imperfection in the current research could be produced by the physical presence of the plasma actuator placed near the leading edge. From Case 6 (Fig. 9g) up to the highest perturbation St_e in

Case 9 (Fig. 11j), there are practically no changes in the shape of the stall cells.

From the results presented so far and the results presented by Dell'Orso (2018), it is clear that standard surface pressure measurements or planar streamwise PIV measurements, with taps and laser sheet normally located on the centerline of the model, could provide erroneous results if significant separation line three-dimensionality or stall cells are present. As such, calculating lift, drag, and moment coefficients for the airfoil based on mid-span measurements can introduce significant errors, but the level of error will depend on the extent of separation over the airfoil, the existence of stall cells, and the location of the pressure taps and laser sheet. For example, the location of surface pressure taps in the current work is indicated by black dotted lines in the FSOFV images of Fig. 7. While the pressure taps are well within the separated flow region in the baseline case, they are situated between the stall cells for Cases 2 and 8, and therefore, the measurements miss the true extent of the separation. In fact, the differences between the lift coefficient results for the clean airfoil and the airfoil with the actuator mounted, shown in Fig. 4, can be partially attributed to this potential three-dimensionally (see Fig. 5). Additionally, keeping in mind that the VR-7 airfoil is a thin airfoil, which generates most of its lift close to the leading edge, the presence of stall cells close to the leading edge is likely to introduce spanwise variations in the wing loading. However, if the stall cells are located away from the leading edge, the airfoil will not likely experience large spanwise variations in loading.

3.3 Discussion of the results

To put the current work into proper context and further discuss the results, a brief discussion of the dynamics of the complex stalled flow over an airfoil is warranted. In such a flow, a free shear layer is riding over a large separated region. While the instability, flow structures, and control of free shear layers have been studied for many decades and their similarities have been observed over a large range of flow speeds and Reynolds numbers (Samimy et al. 2018), the dynamics of the combined flow are much more complex, and are Reynolds number, angle of attack and airfoil aspect ratio dependent. Therefore, most of the recent theoretical work has been focused on low-speed and low Reynolds number laminar flows (He et al. 2017). A few important points on free shear layers include: (1) simple free shear layers are unstable over a large range of Strouhal numbers ($St_\theta = f\theta/U_\infty$, θ is the momentum thickness and U_∞ is the free stream velocity), the most amplified Strouhal number is around 0.032, and the linear Kelvin–Helmholtz instability governs the initial development of the shear layer; (2) the dynamics of free shear layers are dominated by large-scale structures developed due to the K–H instability and they are present even in high Reynolds number turbulent flows; (3) the shear layer responds to active control even in high Reynolds number and Mach number (well into supersonic regime) turbulent flows; and (4) in flows with a second length scale such as in jets, cavity flows, and separated flows, the K–H instability has a second mode which scales with this length scale (e.g., $St = fc/U_\infty$, c is the airfoil chord length in flows over the airfoil), St is an order of magnitude larger than St_θ, and the shedding Strouhal number of the vortices in a stalled flow is around 1 ($St_n \sim 1$).

In the current work with a modest Reynolds number of 500,000 and airfoil aspect ratio 3, the free shear layer dynamics are controlled using perturbations provided by an NS-DBD plasma actuator over a large Strouhal number covering from $0.5St_n$ to $24St_n$, which in turn affects the dynamics of the entire system. Natural vortex shedding was measured to be at $St_n \sim 0.60$ (Esfahani et al. 2016). Excitation at low Strouhal numbers ($St_e \sim St_n$) results in organized, large-scale, coherent structures in the shear layer over the separated region with shedding Strouhal numbers that correspond to that of the excitation, and the shedding of vortices from the leading and trailing edges are synchronized. Convection of these structures over the separated region along the chord of the airfoil and entrainment of high-momentum freestream fluid into the separated zone result in cyclic flow reattachment, the time-averaged result of which is a nearly chordwise spatially uniform increase in suction. In contrast, excitation at higher Strouhal numbers ($St_e \sim 10St_n$) results in much smaller, less coherent structures in the shear layer that quickly develop over the airfoil and disintegrate and thus entrain the freestream flow into the separation zone and reattach the flow only over the first 40% of the cord.

The response of the free shear layer over the separated zone to the excitation is consistent with the excitation of K–H instability in free shear layers and similar to that in other flows containing shear layers such as jets and cavity flows (Samimy et al. 2018). However, changing the nature of flow structures by excitation at different St_e, significantly changes the dynamics of the overall system, including the separation region—excitation at higher St_e leads to the development of stall cells. Unfortunately, there are no stability analyses of such moderately high Reynolds number turbulent flows, therefore, the results are further discussed using the theoretical analyses in much lower Reynolds number laminar flows. The most recent modal and non-modal linear global stability analysis over three different airfoils (thin and thick without camber, and thick with camber), which also provides a good review of the work over the past few decades (He et al. 2017), asserts there are two different mechanisms of linear instability in stalled flows over an airfoil at low Reynolds numbers: the Kelvin–Helmholtz instability mode, which dominates the flow excited by large spanwise wavelength perturbations, and a three-dimensional

stationary mode, which becomes more active as the spanwise periodicity wavelength of the perturbations is reduced. An argument can be made that our results are qualitatively consistent with these findings: at low excitation Strouhal numbers ($St_e \sim St_n$), the excitation promotes coherent structures with large streamwise and spanwise extent, while at high Strouhal number excitation ($St_e \sim 10St_n$), the excitation promotes less coherent structures with much smaller streamwise and spanwise extent. Therefore, in the former case, K–H mode is more amplified suppressing the development of stall cells and in the latter case the three-dimensional stationary mode is more amplified promoting the development of stall cells.

Additional experiments were conducted to shed further light on the physics of the complex stalled flow over an airfoil and to confirm whether the separated flow was globally unstable. The aim was to observe the changes that happen to well-defined stall cells generated by the perturbations when the actuator was deactivated. Therefore, the perturbed flow field of Case 8 was chosen, as it showed well-defined stall cells. Once a steady freestream flow in the tunnel was established, the actuator was turned on and the tunnel was run for approximately 6 min so that a well-defined, steady oil flow pattern would emerge on the surface of the airfoil. The first image was acquired just before the actuator was turned off at $T = t_0$ (Fig. 10a) and subsequent images were taken in 10-s intervals. At $T = t_0 + 10$ (Fig. 10b), the strength of the vortex node impinging at $z/b = -0.1$ is significantly increased and the node is shifted to the left close to $z/b = 0$. Simultaneously, the size of the stall cell on the left half of the airfoil is significantly reduced. This trend is reversed in Fig. 10c–f where the cell continues to grow and the separation line continues to move upstream and is finally stabilized at $T = t_0 + 40$. At the same time, the size of the bigger cell on the right continues to diminish and finally returns to its original shape at $T = t_0$. At $T = t_0 + 30$ (Fig. 10d), a relatively strong vortex node starts to appear at $z/b = 0.4$ and moves to the right while deforming and slightly moving upstream. A stable surface pattern that strongly resembles the initial surface topology at $T = t_0$ emerges at $T = t_0 + 50$ (Fig. 10f).

It appears that turning the actuator off has an initial disrupting effect on the flow field but eventually, after approximately 40 s, the flow reverts to nearly its original equilibrium state that was established due to perturbation. The experiment was repeated with the same result. Even long after the actuator is turned off, the surface topology does not indicate the presence of a quasi-3-D separation front that was seen in the baseline case (Fig. 6a); rather, the signature of the stall cells remains clearly visible. This suggests that the stalled flow over the VR-7 airfoil is globally unstable, similar to very low Reynolds number laminar separated flows in theoretical work (Rodriguez and Theofilis 2010, 2011; Hammond and Redekopp 1998). However, it should be kept in mind that this was done by exciting the
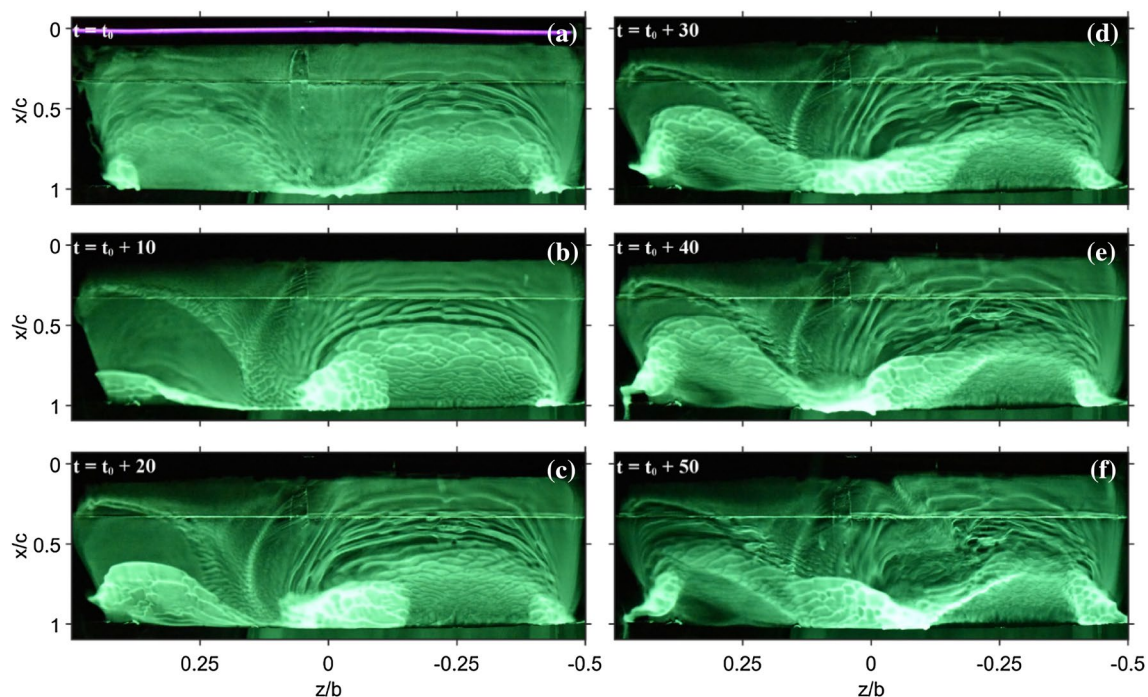

Fig. 10 Series of still FSOFV images acquired at $\alpha = 19°$ and $Re = 500{,}000$ depicting the development of the surface topology pattern after turning off the actuator (for Case 8) at $T = t_0$

K–H instability with $St_e \sim 24 St_n$ generating much smaller and more three-dimensional structures in the shear layer. Therefore, the results are also consistent with the results of He et al. (2017).

The results presented in Sect. 3.2 clearly show the effects of St_e and the results qualitatively agree with the theoretical results of He et al. (2017). Weihs and Katz (1983) postulated that the stall cells are formed due to the excitation of the Crow instability (Crow 1970) whereby the interaction between the vortex lines shed from the shear layer over the separated region and the trailing edge of the airfoil leads to the formation of vortex rings which impinge on the airfoil surface and form the stall cells. The results presented earlier and discussed above, do not seem to agree with this assertion. However, Yon and Katz (1998b) in their study concluded that shear layer roll up is not the mechanism responsible for the formation of stall cells, and the current results seem to support this assertion. A limited number of experiments in which a high Strouhal number perturbation signal is modulated with a low Strouhal number signal was conducted to explore the competition between the two excitation regimes on the flow field. The Strouhal number of the carrier waveform in these experiments was fixed at $St_e = 10.97$, which is very close to Case 8 in Table 1. In all cases, stall cells were clearly present and well-defined similar to those in Fig. 9f–j. A sample result for modulation with Case 2 ($St_e = 0.6$) in Table 1 is presented in Fig. 11 (Case 10 in Table 1). Comparing this velocity field, with the baseline case (Fig. 9a), and the plot for the unmodulated Case 8 (Fig. 9i) clearly shows the relatively small effect of the low St_e modulation.

The choice of showing the result with modulating the carrier signal with the Case 2 ($St_e = 0.6$) is deliberate, as this is the natural shedding Strouhal number of the baseline case and the previous results have shown the most significant effect of the excitation of the shear layer over the separated region at this St_e (Esfahani et al. 2016). In addition, the shedding of shear layer vortices and the trailing edge vortices are synchronized at this excitation Strouhal number. Comparing the flow fields of this modulated case (Case 10) with those of Cases 2 and 8, it is clear that the stall cells are quite similar in Cases 8 and 10 and the flow fields are quite different in Cases 2 and 10. These results indirectly affirm the assertion of Yon and Katz (1998b) that shear layer roll up is not the cause of the formation of stall cells, but not that of Weihs and Katz (1983) that stall cells are formed due to the excitation of the Crow instability.

4 Conclusions

The mushroom-shaped, three-dimensional flow features on the surface of a post-stall airfoil, referred to as stall cells, have been the subject of investigation for over 45 years. Many detailed experimental investigations have shed light on the conditions under which stall cells emerge. While advances in flow diagnostics have helped to further the understanding of the stall cells and their characteristics, the underlying mechanisms that lead to their emergence in post-stall flows are not yet well-understood. Early work postulated that the stall cells are formed due to the excitation of the Crow instability, whereby the interaction between the vortex lines from the shear layer over the separated region and the trailing edge of the airfoil leads to the formation of vortex rings which impinge on the airfoil surface and form stall cells.

It has come to light in recent years that there are some common features of separated flows, regardless of the Reynolds number and Mach number. First, they contain embedded streamwise structures or vortices, such as those generating stall cells in flows over stalled airfoils and separated two-dimensional boundary layers, and Gortler-type streamwise vortices in supersonic shock wave/turbulent boundary layer interactions. Second, the streamwise vortices are unsteady and sensitive to upstream disturbances, but they can be made spatially steady by fixing the location of the upstream
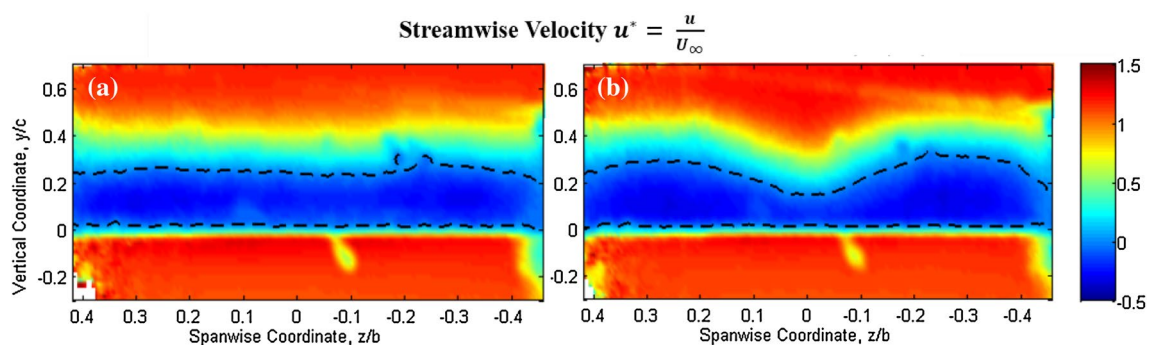

Fig. 11 Color map of normalized ensemble-averaged streamwise velocity on a cross-stream plane at $x/c = 1.05$ at $\alpha = 19°$ and $Re = 500{,}000$ for (**a**) low St_e case (Case 2) and (**b**) high St_e case modulated with low St_e case (Case 10). Dashed black lines indicate zero streamwise velocity

disturbances. This has been done in flows over stalled airfoils and in supersonic shock wave/turbulent boundary layer interactions. Third, there are two main unsteady features in the flow, one is associated with the shedding of vortices over the shear layer and another, which has an order of magnitude smaller in frequency, is likely associated with the unsteady separated-bubble motion. The exact mechanism for the latter is still being debated in literature.

The modal linear global stability analysis of Rodriguez and Theofilis (2011) over a stalled airfoil showed the globally unstable nature of a laminar two-dimensional stalled flow over an airfoil and the dependence of the formation of the stall cells on the amplitude of the perturbations. However, the most recent modal and non-modal linear global stability analysis over three different airfoils (thin and thick without camber, and thick with camber) showed that the Kelvin–Helmholtz instability mode is amplified more strongly than the three-dimensional global mode and the stall cell-like structures are formed by superposition of K–H instability and a secondary instability results.

A VR-7 thin asymmetric airfoil with an aspect ratio $AR = 3$ was used in this work. The composite airfoil had a chord of $c = 20.3$ cm and the angle of attack investigated here was $19°$ at a chord-based Reynolds number of $0.50 \cdot 10^6$. While the tunnel blockage was larger than desirable, the effect on the formation of stall cells due to active perturbation is expected to be negligible, as all the experiments were conducted at a fixed angle of attack and Reynolds number. The active perturbation in this work is generated using nanosecond pulse driven dielectric barrier discharge (NS-DBD) plasma actuators. Previous studies have demonstrated that these actuators mainly affect the flow by generating rapid, localized Joule heating that can excite the K–H instability in the flow. The K–H instability is known to respond to perturbations over a large range of Strouhal number and the perturbation amplitude does not play a significant role beyond a threshold level. In the current experiments, the individual perturbation amplitude is kept constant, as typically done in active flow control, and the Strouhal number changed from approximately $0.5 St_n$ to over $24 St_n$ to ascertain the dependence of the three-dimensionality of the flow field and the existence of stall cells on perturbation Strouhal number.

The baseline flow results show a quasi-3-D separation front over the airfoil. Such separation fronts have been observed by others and suggested to be precursors to the development of well-defined mushroom-shaped stall cells. It has also been shown in the literature that separated flows with a thin approaching boundary layer are susceptible to disruption by any minor surface imperfections. The excitation results show a gradual appearance of stall cells by increasing the perturbation Strouhal number to approximately 3 times the natural shedding Strouhal number of $St_n = 0.6$. The stall cells become well-defined and eventually

saturated with no further changes with increasing perturbation Strouhal number beyond $10 St_n$. It was shown that the instability responsible for the stall cells is self-sustained as the stall cells remain in place after the perturbations are turned off. Additionally, results of experiments conducted with modulated excitation indirectly confirm the assertion of Yon and Katz (1998b) that shear layer roll up is not the cause of stall cell formation, but not that of Weihs and Katz (1983) that stall cells are formed due to the excitation of the Crow instability. The results of the current work are discussed and interpreted using recent modal and non-modal linear global stability analyses, even though they have been carried out in a much lower Reynolds number laminar stalled flows over airfoils.

References

Adamovich I, Little J, Nishihara M, Takashima K, Samimy M (2012) Nanosecond pulse surface discharges for high-speed flow control. In: 6th AIAA flow control conference. AIAA paper 2012–3137

Akins DJ, Singh A, Little JC (2015) Effects of pulse energy on shear layer control using surface plasma discharges. In: 45th AIAA fluid dynamics conference. AIAA paper 2015–3344

Barlow J, Rae W, Pope A (1999) Low-speed wind tunnel testing, 3rd ed. Wiley, Hoboken

Benard N, Moreau E (2010) Capabilities of the dielectric barrier discharge plasma actuator for multi-frequency excitations. J Phys D Appl Phys 43:145201. https://doi.org/10.1088/0022-3727/43/14/145201

Boiko AV, Dovgal AV, Zanin YB, Kozlov VV (1996) Three-dimensional structure of separated flows on wings (review). Thermophys Aeromechanics 3:1–13

Broeren AP, Bragg MB (2001) Spanwise variation in the unsteady stalling flowfields of two-dimensional airfoil models. AIAA J 39:1641–1651. https://doi.org/10.2514/2.1501

Crow SC (1970) Stability theory for a pair of trailing vortices. AIAA J 8:2172–2179. https://doi.org/10.2514/3.6083

Dawson R, Little J (2013) Characterization of nanosecond pulse driven dielectric barrier discharge plasma actuators for aerodynamic flow control. J Appl Phys 113:103302. https://doi.org/10.1063/1.4794507

Dawson RA, Little J (2014) Effects of pulse polarity on nanosecond pulse driven dielectric barrier discharge plasma actuators. J Appl Phys 115:043306. https://doi.org/10.1063/1.4863175

Dell'Orso H, Amitay M (2018) Parametric investigation of stall cell formation on a NACA 0015 Airfoil. AIAA J Article Adv. https://doi.org/10.2514/1.J056850

Dell'Orso H, Chan W, Amitay M (2016a) Induced stall cells on a NACA0015 airfoil using passive and active trips. In: 8th AIAA flow control conference. AIAA paper 2016–3621

Dell'Orso H, Tuna BA, Amitay M (2016b) Measurement of three-dimensional stall cells on a two-dimensional NACA0015 airfoil. AIAA J 54:3872–3883. https://doi.org/10.2514/1.J054848

Demauro EP, Dell'Orso H, Sivaneri V, Tuna B, Amitay M (2015) Measurements of 3-D stall cells on 2-D airfoil. In: 45th AIAA fluid dynamics conference. AIAA paper 2015–2633

Disotell KJ (2015) Low-frequency flow oscillations on stalled wings exhibiting cellular separation topology. The Ohio State University

Disotell KJ, Gregory J (2015) Time-resolved measurements of cellular separation on a stalling airfoil. In: 53rd AIAA aerospace sciences meeting. AIAA paper 2015 – 1501

Disotell KJ, Nikoueeyan P, Naughton JW, Gregory JW (2016) Global surface pressure measurements of static and dynamic stall on a wind turbine airfoil at low Reynolds number. Exp Fluids 57:82. https://doi.org/10.1007/s00348-016-2175-z

Durasiewicz C, Singh A, Little JC (2018) A comparative flow physics study of Ns-DBD vs Ac-DBD plasma actuators for transient separation control on a NACA 0012 airfoil. In: 2018 AIAA aerospace sciences meeting. AIAA paper 2018–1061

Esfahani A, Singhal A, Clifford CJ, Samimy M (2016) Flow separation control over a Boeing Vertol VR-7 using NS-DBD plasma actuators. In: 54th AIAA aerospace sciences meeting. AIAA paper 2016 – 0843

Greenblatt D, Wygnanski I (2003) Effect of leading-edge curvature on airfoil separation control. J Aircr 40:473–481. https://doi.org/10.2514/2.3142

Gregory N, Quincey V, O'Reilly C, Hall D (1971) Progress report on observations of three-dimensional flow patterns obtained during stall development on aerofoils, and on the problem of measuring two-dimensional characteristics

Gross A, Fasel HF, Gaster M (2015) Criterion for spanwise spacing of stall cells. AIAA J 53:272–274. https://doi.org/10.2514/1.J053347

Hammond DA, Redekopp LG (1998) Local and global instability properties of separation bubbles. Eur J Mech B Fluids 17:145–164. https://doi.org/10.1016/S0997-7546(98)80056-3

He W, Gioria RS, Pérez JM, Theofilis V (2017) Linear instability of low Reynolds number massively separated flow around three NACA airfoils. J Fluid Mech 811:701–741. https://doi.org/10.1017/jfm.2016.778

Helm CM, Martin MP (2017) Gortler-like vortices in the LES data of a Mach 7 STBLI. In: 55th AIAA aerospace sciences meeting. AIAA paper 2017–0762

Leonov SB, Petrishchev V, Adamovich IV (2014) Dynamics of energy coupling and thermalization in barrier discharges over dielectric and weakly conducting surfaces on µ s to ms time scales. J Phys D: Appl Phys 47:465201. https://doi.org/10.1088/0022-3727/47/46/465201

Little J (2018) Localized thermal perturbations for control of turbulent shear flows. AIAA J Special Issue

Little J, Takashima K, Nishihara M, Adamovich I, Samimy M (2010) High lift airfoil leading edge separation control with nanosecond pulse DBD plasma actuators. In: 5th flow control conference. AIAA paper 2010–4256

Little J, Takashima K, Nishihara M, Adamovich I, Samimy M (2012) Separation control with nanosecond-pulse-driven dielectric barrier discharge plasma actuators. AIAA J 50:350–365. https://doi.org/10.2514/1.J051114

Manolesos M, Voutsinas SG (2014) Study of a stall cell using stereo particle image velocimetry. Phys Fluids 26:045101. https://doi.org/10.1063/1.4869726

Marino A, Catalano P, Marongiu C, Peschke P, Hollenstein C, Donelli R (2013) Effects of high voltage pulsed DBD on the Aerodynamic performances in subsonic and transonic conditions. In: 43rd fluid dynamics conference. AIAA paper 2013–2752

Martin MP, Priebe S, Helm CM (2016) Upstream and downstream influence on STBLI instability. In: 46th AIAA fluid dynamics conference. AIAA paper 2016–3341

McCullough GB, Gault DE (1951) Examples of three representative types of airfoil-section stall at low speed. NACA-TN-2502. National Advisory Committee for Aeronautics. Ames Aeronautical Lab, Moffett Field

Moreau E (2007) Airflow control by non-thermal plasma actuators. J Phys D Appl Phys 40:605. https://doi.org/10.1088/0022-3727/40/3/S01

Moss GF, Murdin PM (1971) Two-dimensional low-speed tunnel tests on the NACA 0012 section including measurements made during pitching oscillations at the stall. Her Majesty's Stationary Office, Aeronautical Research Council, CP No.1145, May 1971

Nishihara M, Takashima K, Rich JW, Adamovich IV (2011) Mach 5 bow shock control by a nanosecond pulse surface dielectric barrier discharge. Phys Fluids 23:066101. https://doi.org/10.1063/1.3599697

Patel MP, Ng TT, Vasudevan S, Corke TC, Post M, McLaughlin TE, Suchomel CF (2008) Scaling effects of an aerodynamic plasma actuator. J Aircr 45:223–236. https://doi.org/10.2514/1.31830

Peschke P, Goekce S, Leyland P, Ott P, Hollenstein C (2013) Experimental investigation of pulsed dielectric barrier discharge actuators in sub- and transonic flow. In: 44th AIAA plasmadynamics and lasers conference. AIAA paper 2013–2885

Ragni D, Ferreira C (2016) Effect of 3D stall-cells on the pressure distribution of a laminar NACA64-418 wing. Exp Fluids 57:127. https://doi.org/10.1007/s00348-016-2215-8

Rethmel C, Little J, Takashima K, Sinha A, Adamovich I, Samimy M (2011) Flow separation control over an airfoil with nanosecond pulse driven DBD plasma actuators. In: 49th AIAA aerospace sciences meeting. AIAA paper 2011 – 487

Rodríguez D, Theofilis V (2010) Structural changes of laminar separation bubbles induced by global linear instability. J Fluid Mech 655:280–305. https://doi.org/10.1017/S0022112010000856

Rodríguez D, Theofilis V (2011) On the birth of stall cells on airfoils. Theor Comput Fluid Dyn 25:105–117. https://doi.org/10.1007/s00162-010-0193-7

Roupassov DV, Nikipelov AA, Nudnova MM, Starikovskii AY (2009) Flow separation control by plasma actuator with nanosecond pulsed-periodic discharge. AIAA J 47:168–185. https://doi.org/10.2514/1.38113

Samimy M, Kim J-H, Kastner J, Adamovich I, Utkin Y (2007) Active control of high-speed and high-Reynolds-number jets using plasma actuators. J Fluid Mech 578:305–330. https://doi.org/10.1017/S0022112007004867

Samimy M, Webb N, Crawley M (2018) Excitation of free shear layer instabilities for high-speed flow control. AIAA J 56:1770–1791. https://doi.org/10.2514/1.J056610

Schewe G (2001) Reynolds-number effects in flow around more-or-less bluff bodies. J Wind Eng Ind Aerodyn 89:1267–1289. https://doi.org/10.1016/S0167-6105(01)00158-1

Schülein E, Trofimov VM (2011) Steady longitudinal vortices in supersonic turbulent separated flows. J Fluid Mech 672:451–476. https://doi.org/10.1017/S0022112010006105

Spalart PR (2014) Prediction of lift cells for stalling wings by lifting-line theory. AIAA J 52:1817–1821. https://doi.org/10.2514/1.J053135

Takashima K, Zuzeek Y, Lempert W, Adamovich I (2010) Characterization of surface dielectric barrier discharge plasma sustained by repetitive nanosecond pulses. In: 41st plasmadynamics and lasers conference. AIAA paper 2010–4764

Takashima (Udagawa) K, Zuzeek Y, Lempert WR, Adamovich IV (2011) Characterization of a surface dielectric barrier discharge plasma sustained by repetitive nanosecond pulses. Plasma Sources Sci Technol 20:055009. https://doi.org/10.1088/0963-0252/20/5/055009

Theofilis V, Hein S, Dallmann U (2000) On the origins of unsteadiness and three-dimensionality in a laminar separation bubble. Philos Trans R Soc A Math Phys Eng Sci 358:3229–3246. https://doi.org/10.1098/rsta.2000.0706

Weihs D, Katz J (1983) Cellular patterns in poststall flow over unswept wings. AIAA Journal 21:1757–1759. https://doi.org/10.2514/3.8321

Winkelmann AE (1982a) An experimental study of mushroom shaped stall cells. In: 3rd joint thermophysics, fluids, plasma and heat transfer conference. AIAA paper 1982 – 942

Winkelmann AE, Barlow JB (1980) Flowfield model for a rectangular planform wing beyond stall. AIAA Journal 18:1006–1008. https://doi.org/10.2514/3.50846

Winkelmann AE, Ngo HT, deSeife RC (1982b) Some observations of separated flow on finite wings. In: 20th aerospace sciences meeting. AIAA paper 1982–346

Yon SA, Katz J (1998a) Cellular structures in the flow over the flap of a two-element wing. J Aircr 35:230–232. https://doi.org/10.2514/2.2288

Yon SA, Katz J (1998b) Study of the unsteady flow features on a stalled wing. AIAA J 36:305–312. https://doi.org/10.2514/2.372